Journal of
Materials Chemistry B

Materials for biology and medicine

Accepted Manuscript

This article can be cited before page numbers have been issued, to do this please use: Q. Sun, X. Zhou, K. wang, T. Sun and Z. Xie, *J. Mater. Chem. B*, 2025, DOI: 10.1039/D5TB01048A.

ROYAL SOCIETY OF CHEMISTRY

rsc.li/materials-b

View Article Online
DOI: 10.1039/D5TB01048A

ARTICLE

Near infrared-triggered diketopyrrolopyrrole nanoparticles for photothermal applications against bacterial infections

Received 00th January 20xx,
Accepted 00th January 20xx

DOI: 10.1039/x0xx00000x

Qijia Sun,[a] Xijia Zhou,[a] Ke Wang,*[a] Tingting Sun,*[b] Zhigang Xie[b]

Abstract Wound infection caused by bacteria is an important reason that affects the rapid healing of wounds, and the emergence of drug-resistant strains makes the treatment more complicated, which brings great challenges to surgeons. To this end, a DPP derivative (DPP-S) with donor-acceptor-donor (D-A-D) structure has been synthesized, which has near-infrared (NIR) absorption spectrum by introducing thione groups, and exhibits excellent photothermal properties under NIR laser irradiation. DPP-S mediated phototherapy can not only effectively inhibit and destroy *Staphylococcus aureus* and *Escherichia coli* biofilm, but also inhibit and destroy methicillin-resistant *Staphylococcus aureus* biofilm. In a mouse wound infection model, DPP-S-mediated photothermal therapy can effectively fight bacterial infection, promote the formation of new blood vessels and the deposition of collagen fibers, and thus accelerate wound healing. This discovery is of great significance for the development of new photothermal agents and also provides a new direction and possibility for the treatment of clinical infectious diseases.

Introduction

In surgical patients, wound infection and poor wound healing are often caused by various bacteria and have become one of the major problems faced by clinicians.[1, 2] Although antibiotics are the first choice for the treatment of bacterial infections, there are limitations in their clinical applications, such as the side effects and lack of specificity. More seriously, due to the widespread use of antibiotics, many bacteria gradually develop resistance, making conventional antibiotics ineffective.[3-5] The emergence of drug-resistant bacteria complicates the treatment of common infections and also leads to increased healthcare costs and poor patient outcomes. Therefore, it is particularly important to develop novel antimicrobial treatments to replace conventional antibiotics.

At present, researchers have proposed a series of antibiotic replacement strategies, including photodynamic therapy (PDT),6, 7 photothermal therapy (PTT),[8-10] gas therapy,[11] photocatalytic therapy,[12] sonodynamic therapy,[13,14] and combination therapies. The high temperature generated by PTT leads to the denaturation of nucleic acids and proteins as well as cell lysis, which can effectively destroy the complete structures of bacteria, making it easier for antibacterial agents to penetrate and eradicate the bacteria. In addition, PTT can prevent bacteria from developing drug resistance through metabolic regulation or the proton pump pathway because it can act on multiple cellular components simultaneously, making it difficult for bacteria to develop drug resistance.[15-18] Studies have shown that PTT can also induce a 'hot spring effect' in local tissues, promoting the proliferation and differentiation of fibroblasts and endothelial cells, thus benefitting the formation of new blood vessels and the healing of wound tissues.[19-22]

Photothermal agents (PTAs) play a crucial role in PTT. Researchers have worked to develop PTAs with NIR absorption, as the NIR laser is more penetrating to tissue and less absorbed by water and hemoglobin.[23-25] Diketopyrrolopyrrole (DPP) is a small-molecule organic dye that has attracted the attention of researchers due to a number of favorable characteristics, including its excellent photophysical properties, tunable structures, and excellent photostability.[26-29] As a π-conjugated organic molecule with an endocannabinoid structure, DPP is capable of forming a donor-acceptor-donor structure, which enables the flexible tuning of its photophysical properties.[30-34] Certain DPP derivatives exhibit intrinsic advantages, including NIR absorption and robust fluorescence emission, which render them highly promising in phototherapy and fluorescence imaging (FLI).[35] Consequently, DPP derivatives demonstrate significant scientific value and potential in phototherapy applications.

In this study, dithiopheneboronic acid was chosen as the electron donor to facilitate the electron transfer of DPP, which led to the successful synthesis of DPP3. For further experiments on the red shift of the absorption spectrum of DPP3, the carbonyl group was subjected to thiolation reaction, leading to the final synthesis of DPP-S. DPP-S was then encapsulated in distearoylphosphatidylethanolamine-polyethylene glycol 2000 (DSPE-PEG_{2000}) to form nanoparticles (DPP-S NPs) for evaluation of its therapeutic efficacy against infection (Scheme 1). Three common clinical pathogenic strains (*Staphylococcus aureus* (*S. aureus*), *Escherichia coli* (*E. coli*), and methicillin-resistant *S. aureus* (MRSA))

[a] Department of Respiratory and Critical Care Medicine, The Second Hospital of Jilin University, Changchun, Jilin 130041, P. R. China.
[b] Key Laboratory of Polymer Ecomaterials, Changchun Institute of Applied Chemistry, Chinese Academy of Sciences, Changchun, Jilin 130022, P. R. China.

View Article Online
DOI: 10.1039/D5TB01048A

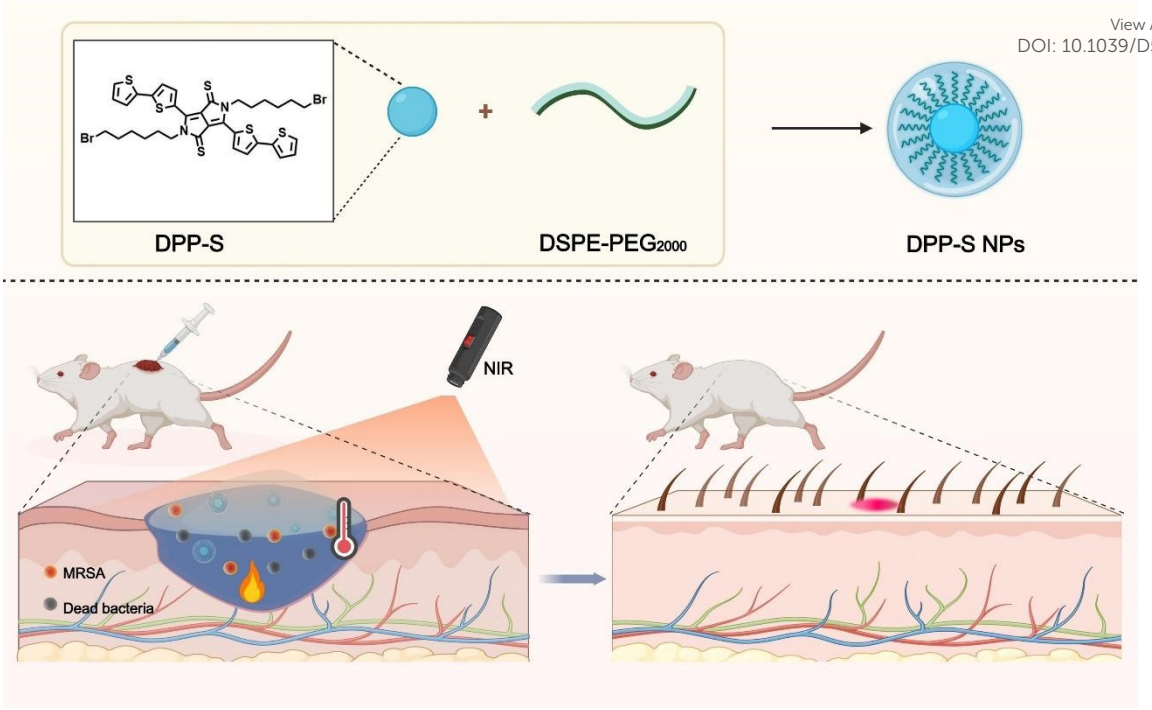

Scheme 1 Schematic representation of the antimicrobial application of DPP-S NPs.

were selected. Under NIR laser irradiation, the nanoparticles demonstrated excellent photothermal effects and were able to efficiently inhibit the growth of bacteria. In the wound infection model of mice, bacterial proliferation was markedly suppressed by DPP-S-mediated PTT treatment, while the formation of new blood vessels and collagen fibers was significantly enhanced, thereby expediting wound healing.

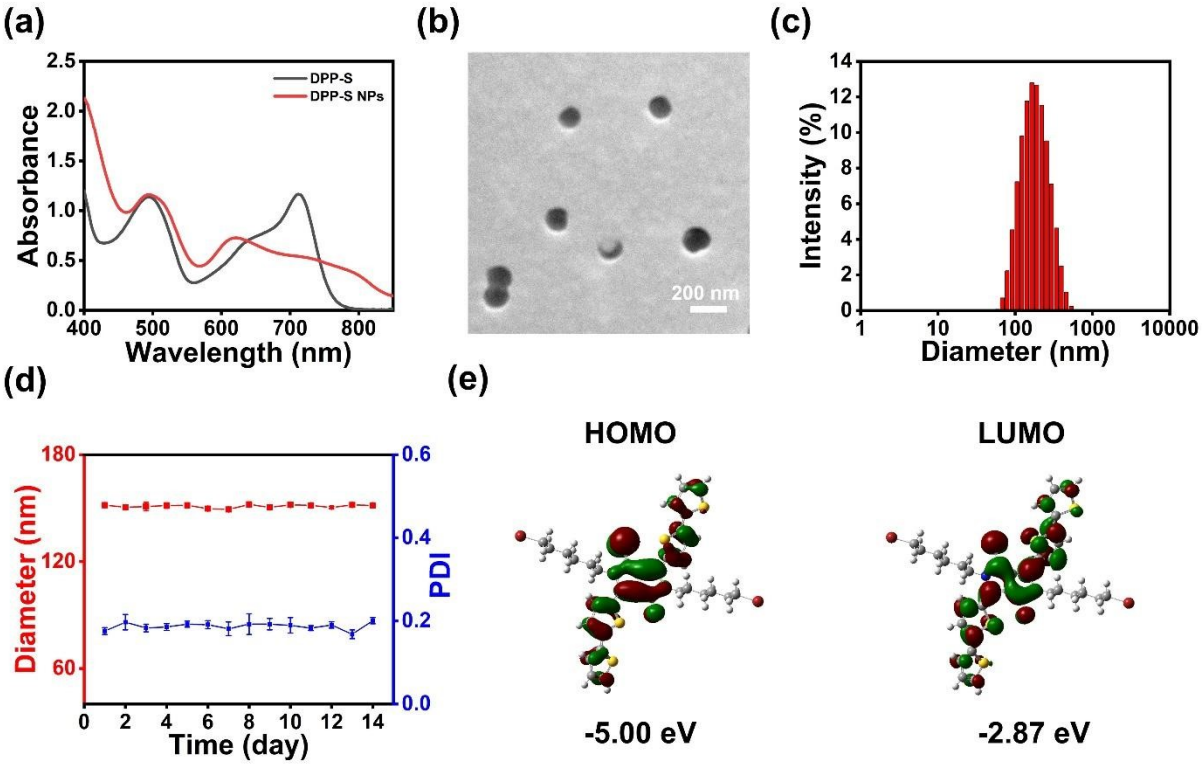

Fig. 1 Characterization of DPP-S NPs. (a) Absorption spectra of DPP-S in N, N-dimethylformamide and DPP-S NPs in water. (b) TEM image of DPP-S NPs. (c) Size distribution of DPP-S NPs characterized by DLS. (d) Changes in sizes and PDIs of DPP-S NPs after storage in water for 14 days. (e) HOMO–LUMO energy level diagrams of the corresponding units of the DPP-S.

View Article Online
DOI: 10.1039/D5TB01048A

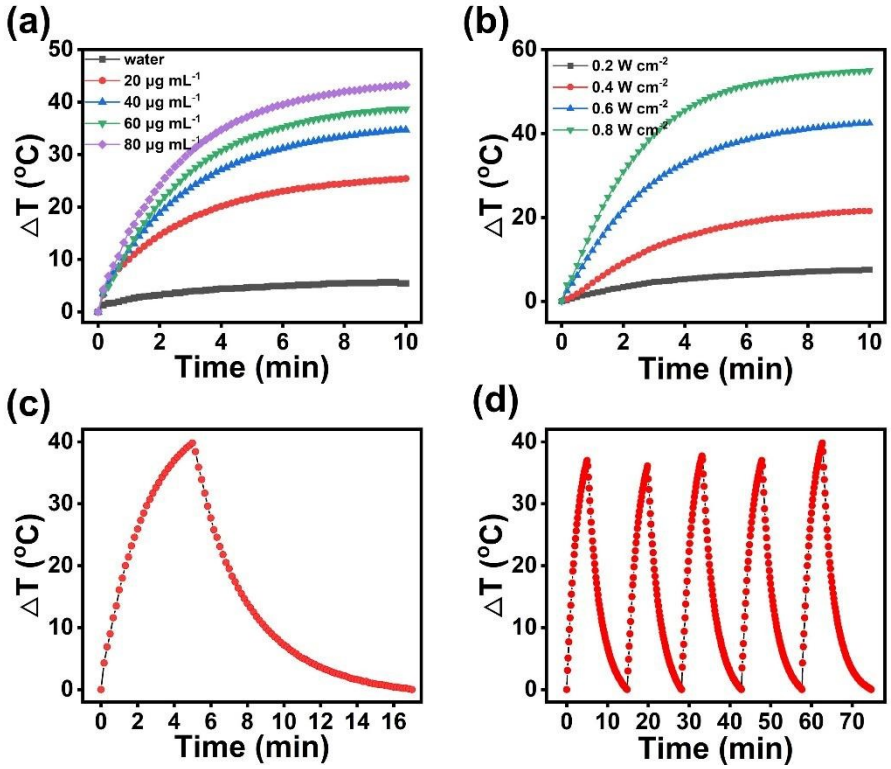

Fig. 2 Photothermal properties of DPP-S NPs. (a) Temperature changes of DPP-S NPs at different concentrations. (b) Temperature variations of DPP-S NPs under irradiation of different laser power densities. (c) Heating and cooling curve of DPP-S NPs. (d) 5 cycles of irradiation and cooling of DPP-S NPs.

Result and discussion

Preparation and characterization of NPs

The synthesis of DPP-S involves 5 steps (Fig. S1). The intermediate DPP1 and DPP2 was first synthesized according to a predetermined method,[36] followed by the reaction with dibenzothiophene boronic acid to obtain DPP3. DPP3 was then reacted with 2,4-bis(4-methoxylphenyl)-1,3-dithia-2,4-diphosphetane-2,4-disulfid (Lawson reagent, LR) to generate the final product DPP-S. The molecular structures of DPP3 and DPP-S were confirmed by ^{1}H NMR spectra (Fig. S2 and S3). The structure of DPP-S was further characterized by ^{13}C NMR (Figure S4) and mass spectrometry (MS) (Fig. S5). Compared with DPP3, the absorption spectrum of DPP-S shows an obvious redshift (Fig. S6). DSPE-PEG$_{2000}$ was utilized to prepare DPP-S NPs via a nanoprecipitation method. DPP-S NPs have a broader absorption spectrum compared to DPP-S (Fig. 1(a)). Transmission electron microscopy (TEM) results show that DPP-S NPs have a regular spherical shape (Fig. 1(b)). Dynamic light scattering (DLS) analysis shows that the average diameter of DPP-S NPs is 147.0 nm (Fig. 1(c)) with a polydispersity index (PDI) of 0.18. The zeta potential of DPP-S NP s was measured at -2.33 Mv (Fig. S7). Furthermore, the particle size and PDI of DPP-S NPs in aqueous solution remained stable over a 14-day monitoring period (Fig. 1(d)), demonstrating good colloidal stability. The electron density distributions of the highest occupied molecular orbital (HOMO) and lowest unoccupied molecular orbital (LUMO) of DPP-S are shown in Fig. 1(e), with a corresponding band gap of 2.13 eV.

Photothermal performances of DPP-S NPs

The photothermal performance of DPP-S NPs was explored under 730 nm laser irradiation. After 10 min of irradiation at a laser power density of 0.6 W cm^{-2}, the temperature of water only increased by 5.6 °C, while the temperature increase (△T) of the DPP-S NPs at a concentration of 80 μg mL^{-1} reached 43.3 °C. Moreover, the temperature changes are closely related to the concentrations of DPP-S NPs. As shown in Fig. 2(a), under the same laser irradiation, DPP-S NPs at different concentrations exhibit obvious temperature differences. In addition, the temperature increase of DPP-S NPs is also related to the laser power densities. As shown in Fig. 2(b), when the concentration of DPP-S NPs is 80 μg mL^{-1}, △T gradually increases as the laser power density increases. Combined with the photothermal cooling curve, we calculated that the PCE of DPP-S NPs was 38.7 % (Fig. 2(c) and S8). During five cycles, the solution temperature of DPP-S NPs can recover to its initial level, whereas the control ICG solution exhibited a substantially decreased temperature following multiple irradiation treatments (Fig. 2(d), S9). This performance demonstrates the excellent photothermal stability of DPP-S NPs. The above results reveal that DPP-S NPs have excellent photothermal performances, which provides the feasibility in the treatment of bacterial infections.

In Vitro Antibacterial Performances of DPP-S NPs

The excellent photothermal properties of DPP-S NPs prompted us to investigate their antibacterial effects. We first selected *S. aureus* and *E. coli* to evaluate their antibacterial effects. The minimum inhibitory concentrations (MICs) of DPP-S NPs under laser irradiation are 60 μg

View Article Online
DOI: 10.1039/D5TB01048A

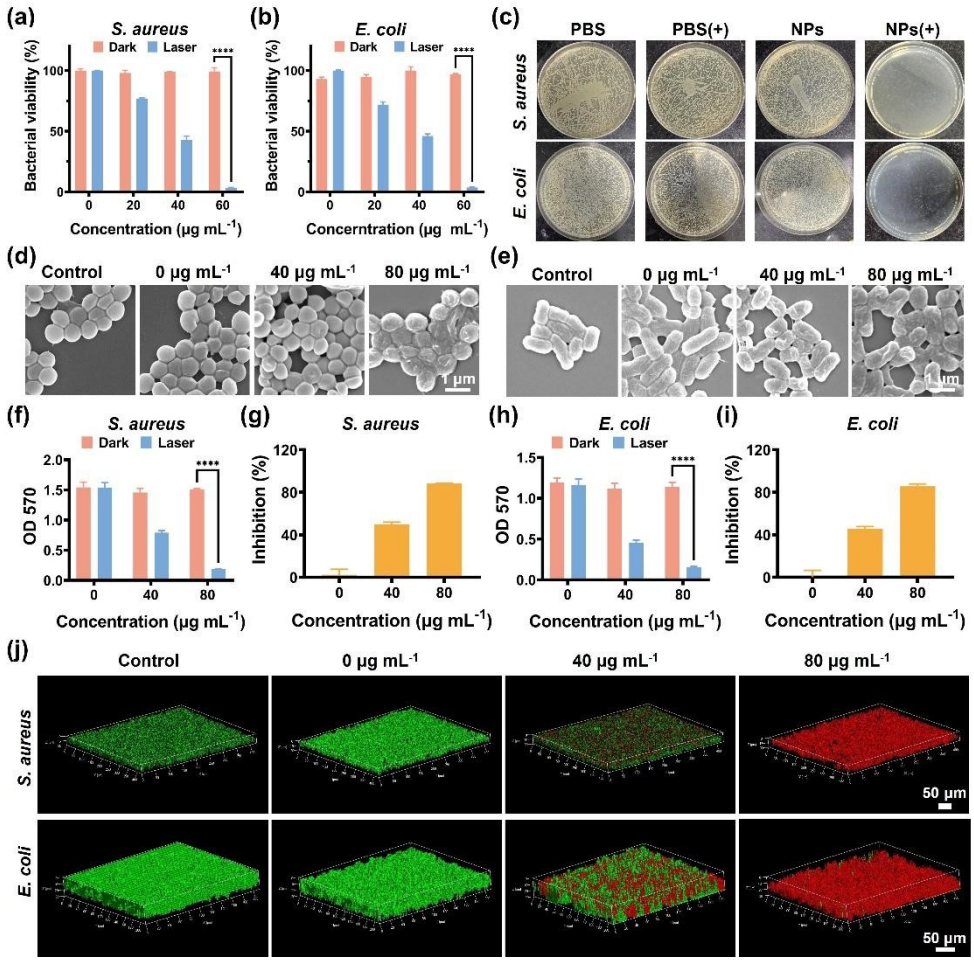

Fig 3 In vitro antimicrobial effects of DPP-S NPs. Survival rates of (a) *S. aureus* and (b) *E. coli* treated with different concentrations of DPP-S NPs under different conditions. (c) Images of representative agar plates of *S. aureus* and *E. coli* after different treatments. SEM images of (d) *S. aureus* and (e) *E. coli* after different treatments. OD570 values of (f) *S. aureus* and (h) *E. coli* after different treatments. Biofilm inhibition of (g) *S. aureus* and (i) *E. coli* treated with different concentrations of DPP-S NPs after laser irradiation. (j) 3D confocal laser scanning microscopy images of *S. aureus* and *E. coli* biofilms after different treatments.

mL^{-1} toward both bacteria (Fig. 3(a), (b) and S10). In addition, when the bacterial suspensions after different treatments were spread on agar plates, almost no colonies existed in the DPP-S NPs combined laser group (NPs(+)), indicating that the NPs can effectively kill *S. aureus* and *E. coli* under laser irradiation (Fig. 3(c)). These results preliminarily demonstrate that DPP-S NPs combined with laser irradiation could effectively inhibit bacterial growth and kill bacteria at a certain concentration. Scanning electron microscopy (SEM) was then used to observe the morphological changes of the bacteria in the different treatment groups. It was not difficult to see that *S. aureus* and *E. coli* in the control group showed regular round or rod-like structures, whereas the morphology of the bacteria appeared to be obviously wrinkled and deformed with the increase in the concentration of DPP-S NPs (Fig. 3(d) and 3(e)).

Biofilm is a membrane structure composed of various substances that can effectively protect bacteria from adverse external factors such as antibiotics.[37, 38] At the same time, the enzymes and small molecular substances rich in the internal structure of the biofilm provide a stable living environment for bacteria.[39] Therefore, the inhibition and destruction of bacterial biofilms is a key step in antibacterial treatment. We evaluated the inhibitory ability of different concentrations (0, 40, and 80 μg mL^{-1}) of DPP-S NPs under laser irradiation on *S. aureus* and *E. coli* biofilms by using crystal violet staining method. As shown in Fig. S11, the biofilm in the control group was thick and relatively intact, whereas the biofilm in the DPP-S NPs combined with laser irradiation group thinned and gradually disappeared with increasing concentration of the nanoparticle solution. The OD570 value of the crystal violet staining solution was consistent with the above results (Fig. 3(f)). When DPP-S NPs were combined with laser irradiation, the inhibition rate of the 40 μg mL^{-1} nanoparticle against *S. aureus* biofilm was only 49.8 %, while the biofilm inhibition rate of the 80 μg mL^{-1} nanoparticle solution treatment group against *S. aureus* was 88.1 % (Fig. 3(g)). Similarly, inhibition of biofilm formation was also achieved against *E. coli* (Fig. 3(h)）, S11, and 3(i)).

Furthermore, the efficacy of DPP-S NP-mediated phototherapy against mature biofilms was continuously verified through bacterial live/dead staining. The three-dimensional (3D) structure of the

View Article Online
DOI: 10.1039/D5TB01048A

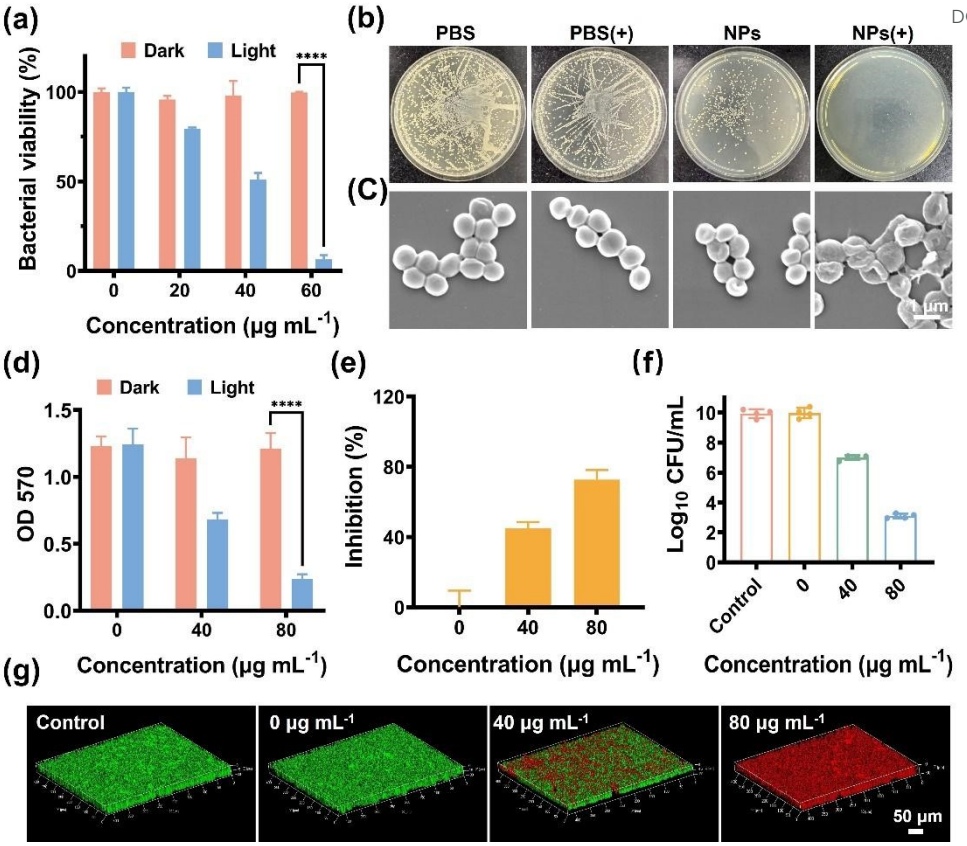

Fig. 4 Antimicrobial properties of DPP-S NPs against MRSA. (a) Survival rate of MRSA. (b) Images of representative agar plates of MRSA after different treatments. (c) SEM images of MRSA after different treatments. (d) OD 570 values of crystal violet staining solutions of different treatment groups. (e) Inhibition rates of MRSA biofilms by DPP-S NPs. (f) Quantitative analysis of bacteria in biofilm after different treatments. (g) 3D confocal laser scanning microscopy images of MRSA biofilms after different treatments.

biofilm showed that both *S. aureus* and *E. coli* in the control group showed a distinct green fluorescence, and at a concentration of 40 μg mL^{-1} of DPP-S NPs (Fig. 3(j)), a mixed fluorescence of red and green was seen, indicating that a significant number of viable bacteria were still present. When the concentration reached 80 μg mL^{-1}, the majority of the bacteria in the biofilm were died (Fig. 3(h)). In addition, total bacterial counts of the treated suspensions were performed by standard plate counting and the results were suppressed with the above results (Fig. S12). This implies that DPP-S NPs can effectively disrupt mature biofilms. The above results indicate that DPP-S NP-mediated phototherapy can effectively inhibit and destroy bacterial biofilms.

Currently, most clinically detected *S. aureus* strains are drug-resistant, especially MRSA with broad-spectrum resistance.[40] Motivated by the previous experiments, we further evaluated the antibacterial performance of DPP-S NPs against MRSA. As shown in Fig. 4(a), the survival rate of bacteria does not change much under dark conditions. However, under laser conditions, as the concentration of DPP-S NPs increases, the survival rate of MRSA gradually decreases, indicating that DPP-S NPs combined with laser irradiation is also effective against MRSA. Additionally, the MIC of DPP-S NPs against MRSA was also determined to be 60 μg mL^{-1} (Fig. 4(a), S10). When the bacterial fluids after different treatments were spread on agar plates, it could be seen that the combined laser group of DPP-S NPs (NP(+)) was able to kill the bacteria, confirming their antibacterial properties against MRSA (Fig. 4(b)). SEM results of the nanoparticles combined with the light group showed obvious crumpling and deformation, which also supported the above conclusion (Fig. 4(c)).

Next, we measured the inhibitory ability of DPP-S NPs against MRSA biofilms. When the concentration of DPP-S NPs reached 80 μg mL^{-1}, the absorbance of the crystal violet staining solution at 570 nm was significantly lower than that of the control group, with an inhibition rate of 72.7 % (Fig. 4(d), (e), and S13). Live/dead staining experiments and semiquantitative analysis of residual bacteria in the biofilms demonstrated that DPP-S NPs mediated PTT was able to effectively disrupt mature MRSA biofilms and kill bacteria (Fig. 4(g, f)). Taken together, DPP-S NPs combined with laser irradiation can effectively inhibit and destroy the biofilms of *S. aureus*, *E. coli*, and MRSA, demonstrating the broad-spectrum antimicrobial activity of PTT.

In vivo antimicrobial effect

In light of the in vitro antibacterial capabilities of DPP-S NPs, we evaluated their therapeutic efficacy in a mouse wound infection model. Fig. 5(a) indicated that the temperature of the wounds in the DPP-S NPs combined laser group (NPs(+)) group reached above 55 °C during irradiation. In contrast, the temperature of the wounds in the

View Article Online
DOI: 10.1039/D5TB01018A

PBS combined with laser irradiation group (PBS(+)) only increased to about 35 ºC. Photographs were taken to record the changes in the wounds (Fig. 5(b)), and the wound trajectory was simulated using Image J software (Fig. 5(c)). In comparison to the other groups, pronounced wrinkling and scabbing of the wounds in the NPs(+) group were observed on the first day post-treatment, and the wound healing rate reached 95.8 % by the 7th day (Fig. 5(d)). Furthermore, residual bacteria cultures revealed that the colony counts of the bacteria in the NPs(+) group were significantly lower than those in the other three groups (Fig 5(e)).

the wounds in the NPs(+) group, characterized by well-organized skin epidermis and dermis with reduced inflammatory cell infiltration (Fig 5(f)). Additionally, CD31 fluorescence intensity markedly increased in NPs(+) treated wounds, suggesting a significantly higher vascular density (Fig. 5(f)). Collectively, these findings suggest that DPP-S NP-mediated photothermal therapy accelerates wound healing and provides a unique advantage in the treatment of bacterial wound infections.

In vitro and in vivo biosafety assessment

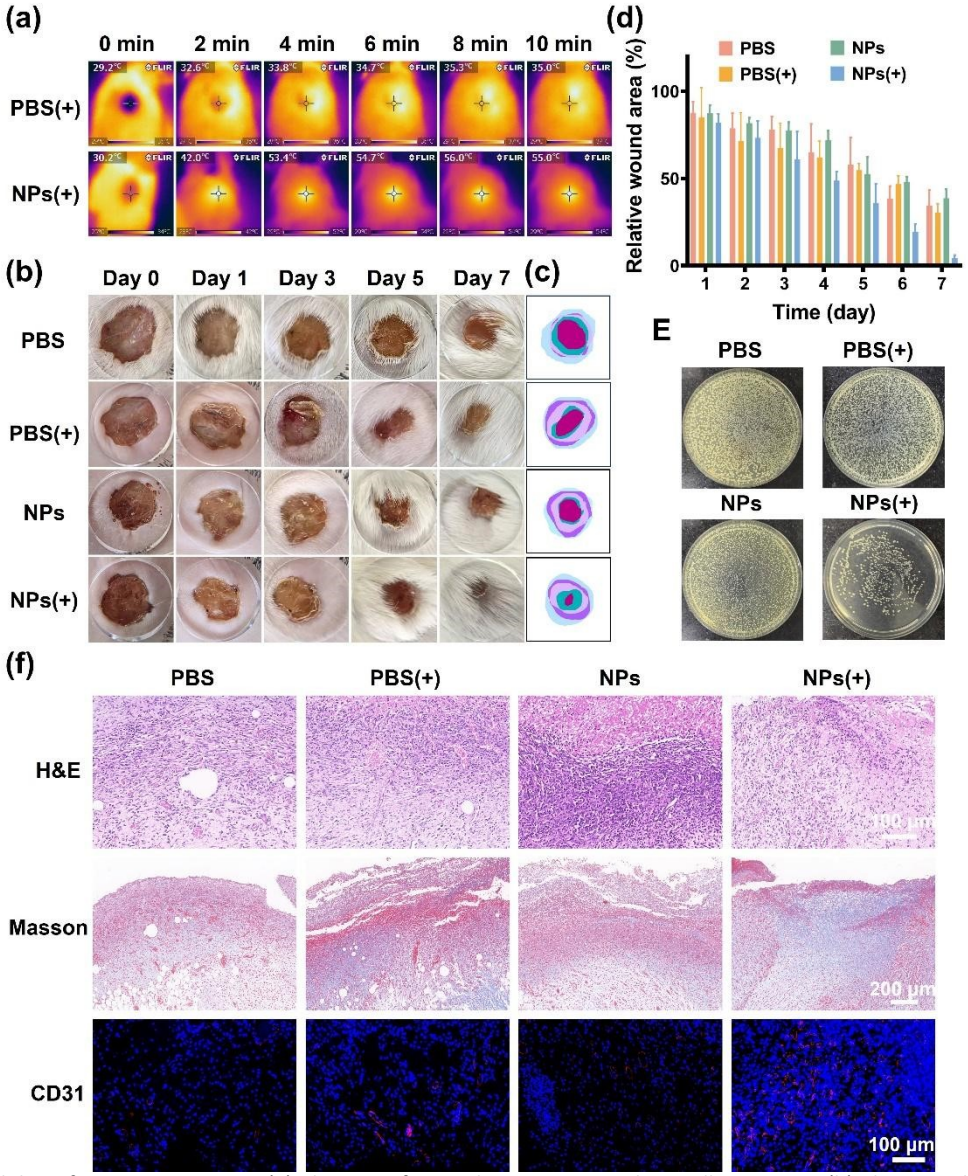

Fig. 5 Antibacterial ability of DPP-S NPs in vivo. (a) Changes of wound temperatures during illumination. (b) Photographs of the wounds of the mice under various treatments on the 0, 1st, 3th, 5th, and 7th days. (c) Simulated wound images on different times during treatments. (d) Relative wound areas during the treatment processes. (e) Agar plates of residual bacteria in wounds. (f) H&E, Masson, and CD31 staining of the wounds after different treatments.

H&E staining of the wound tissues in different treatment groups demonstrated that the NPs(+) group exhibited minimal infiltration of inflammatory cell alongside a substantial number of newly formed hair follicles (Fig 5(f)). Masson staining analysis on the wounds after treatments illustrated considerable collagen fiber deposition within

To evaluate the in vitro cytotoxicity, mouse fibroblast (L929) and mouse embryonic fibroblast (NIH 3T3) cells were selected and tested by 3-(4,5-Dimethylthiazol-2-yl)-2,5-diphenyltetrazolium bromide (MTT) assays. DPP-S NPs showed good biocompatibility with cell viabilities above 80 % at all concentrations (0 - 100 μg mL^{-1}) tested

View Article Online
DOI: 10.1039/D5TB01048A

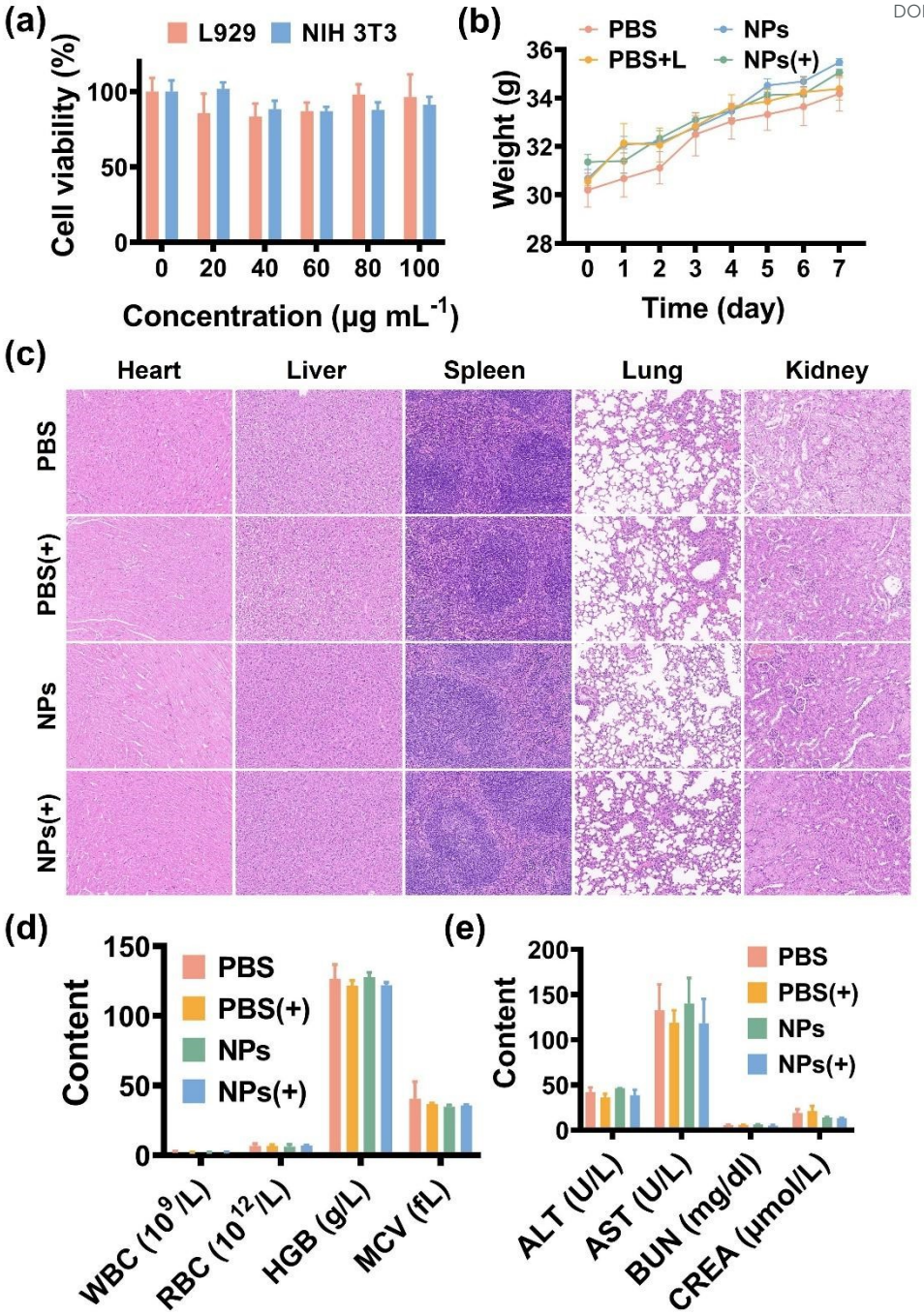

Fig. 6 Biological safety of DPP-S NPs. (a) Cytotoxicity of DPP-S NPs. (b) Changes of body weights of the mice. (c) H&E staining of sections of major organs of the mice in various groups. (d) Blood routine parameters in each group of mice. (e) Biochemical indexes in various groups of mice.

(Fig. 6(a)). The body weights of the mice showed an increasing trend after treatments, and the histological structures of the major organs (heart, liver, spleen, lung, and kidney) remained normal (Fig. 6(b) and (c)). In addition, routine blood parameters (white blood cells (WBC), red blood cells (RBC), hemoglobin (HGB), and mean corpuscular volume (MCV)) and biochemical indexes ((glutamic-pyruvic aminotransferase (ALT), glutamic-oxaloacetic aminotransferase (AST), blood urea nitrogen (BUN), and creatinine (CREA)) were measured on day 7, which indicated that DPP-S NPs had no obvious effect on the hemopoietic system, liver function, and kidney function(Fig. 6(d)). These results indicate that DPP-S NPs treated mice have good biosafety.

Conclusion

In conclusion, we introduced various groups based on DPP and found that its absorption spectrum was significantly red-shifted. This DPP derivative with NIR absorption was confirmed to have excellent photothermal properties. The DPP-S NPs-mediated photothermal treatment showed good killing effect against *S. aureus* and *E. coli*. More importantly, it has the same apparent inhibitory effect on

MRSA. In the MRSA-induced wound infection model, the DPP-S NPs-mediated photothermal effect could effectively inhibit bacterial growth and accelerate the wound healing process. These results indicate that this NIR photothermal material has considerable potential in the treatment of MRSA-induced infections, and is expected to play an important role in clinical applications.

Experiments

Preparation of DPP-S NPs

DPP-S (1 mg) and DSPE-PEG_{2000} (5 mg) were completely dissolved in tetrahydrofuran and then slowly dripped in deionised water, and DPP-S NPs were obtained by stirring and dialysis.

Photothermal properties of DPP-S NPs

To evaluate the photothermal behavior of DPP-S NPs, temperature-time curves and images were recorded. First, different concentrations of NPs (20, 40, 60 and 80 μg mL-1) were exposed to 0.6 W cm-2 of NIR laser (730 nm). Second, NPs (80 μg mL-1) were exposed to NIR light (730 nm) with power densities of 0.4, 0.6, and 0.8 W cm-2. Finally, NPs (80 μg mL-1) were exposed to NIR light (730 nm, 0.6 W cm-2) for 5 heating-colling cycles to study the stability of DPP-S NPs. All the data were collected every 10 s by using an infrared thermal imager. The photothermal conversion efficiency was calculated via the following formula[42]:

$$\eta = \frac{hS(T_{max} - T_{surr}) - Q_o}{I(1-10^{-A_{730}})} \quad (1)$$

$$\tau_s = \frac{C_d m_d}{hS} \quad (2)$$

$$Q_o = hS(T_{max,water} - T_{surr}) \quad (3)$$

The value of τs can be calculated from the linear egression curve in the cooling curve. md and Cd represent the mass of the solution (above 0.4 g) and the heat capacity (4.2 J g^{-1} K^{-1}), respectively. $T_{max,water}$ and T_{surr} respectively represent the maximum temperature of water and the ambient room temperature. T_{max} represents the maximum temperature of the DPP-S NPs solution, while I and A730 respectively denote the laser power (0.6 W cm^{-2}) and the absorbance of DPP-S NPs at 730 nm.

Bacterial culture

Individual colonies of *S. aureus*, *E. coli,* or MRSA on agar plates were transferred to 3 mL of Luria-Bertani (LB) broth medium and shaken for 8 h at 37 °C. The bacteria were harvested and washed twice with phosphate buffer solution (PBS). Then, the bacteria were diluted with PBS to 10^9 CFU mL^{-1} (optical density at 600 nm (OD600) of 1.0).

Minimum Inhibitory Concentration (MIC)

Different concentrations of DPP-S NPs and bacterial suspension were incubated in an incubator at 37 °C for 30 min, followed by irradiation with or without laser (0.6 W cm^{-2}) for 10 min, and the survival rate of bacteria was calculated after 24 h of culture in an incubator at 37 °C.

In vitro inhibition on biofilms

Bacterial suspensions at a final concentration of 10^7 CFU mL^{-1} were incubated with different concentrations of DPP-S NPs for 30 min at 37 °C. The samples were irradiated with or without NIR laser for 10 min, followed by incubation for 24 h in a 37 °C incubator. The medium was removed from the well plates and each well was washed with PBS to remove planktonic bacteria. The wells were then stained with 0.1 % crystal violet for 30 min, rinsed three times with PBS, dried, and photographed. Finally, glacial acetic acid solution was added and allowed to stand for 5 min. The OD570 value was measured to evaluate the degree of biofilm inhibition by DPP-S NPs.

Live/Dead staining assay

The bacterial suspension was diluted to 10^7 CFU mL^{-1} and cultured in an incubator at 37 °C for 48 h. After rinsing twice with PBS, NPs or PBS were added, followed by laser (0.6 W cm^{-2}) irradiation or no irradiation for 10 min. The SYTO/PI staining solution was added, and the survival of bacteria in the biofilms was observed with CLSM.

In vitro cytocompatibility of DPP-S NPs

The mouse fibroblast (L929) and embryonic fibroblast (NIH 3T3) cells were inoculated into 96-well plates and cultured in DMEM medium containing 10 % fetal bovine serum at 37 °C in a 5 % CO_2 incubator. Various concentrations of NPs were then added, followed by MTT solution after 24 h and DMSO solution after 4 h. The OD values of each well were measured.

In vivo infected wound healing evaluation

All animal experiments were approved by the Ethics Committee of Changchun Institute of Applied Chemistry, Chinese Academy of Sciences (approval number: 2024-00104).

Healthy Kunming mice were randomly divided into PBS group, PBS combined with laser irradiation group (PBS(+)), DPP-S NPs group (NPs), and DPP-S NPs combined laser group (NPs(+)). All mice were anesthetized, and their backs were shaved, and a full circular trauma (1 cm in diameter) was created on the back of each mouse. MRSA (1 × 10^8 CFU mL^{-1}, 50 μL) was added to the wounds. 24 h later, the nanoparticle solution or an equivalent amount of PBS was dropped onto the wounds. The infected wounds were irradiated with laser (0.6 W cm^{-2}, 730 nm) for 10 min, and the temperature of the wounds was monitored with an infrared thermal imager. Photographs were taken to record changes in the area of the wounds. All mice were killed on day 7 and wound tissues and organs (heart, liver, spleen, lung, and kidney) were fixed with 4 % paraformaldehyde. Histopathological methods such as hematoxylin and eosin (H&E), Masson and CD31 immunofluorescence staining were used to further evaluate wound healing.

Author contributions

Qijia Sun: Methodology, Investigation, Writing – original draft. Xijia Zhou: Investigation. Ke Wang: Resources, Supervision. Tingting Sun: Conceptualization, Resources, Supervision. Zhigang Xie: Conceptualization, Resources, Supervision.

Conflicts of interest

The authors declare that they have no known competing financial interests or personal relationships that could have appeared to influence the work reported in this paper.

Data availability

Data will be made available on request.

Acknowledgements

This study was supported by Disciplinary Crossing and Integration and innovation project of Norman Bethune Health Science Center of Jilin University (2022JBGS07), and Research and Development of Key Medical Technologies of Jilin Science and Technology Department(20240305080YY), and Jilin Provincial Natural Science Foundation Provincial-Local-Enterprise Joint Fund (Group B) (YDZJ202501ZYTS317).

References

1 L. Yang, D. Zhang, W. Li, H. Lin, C. Ding, Q. Liu, L. Wang, Z. Li, L. Mei, H. Chen, Y. Zhao, X. Zeng, Nat Commun, 14 (2023) 7658.
2 T. Wang, Y. Li, E.J. Cornel, C. Li, J. Du, ACS Nano, 15 (2021) 9027-9038.
3 M. Dai, W. Ouyang, Y. Yu, T. Wang, Y. Wang, M. Cen, L. Yang, Y. Han, Y. Yao, F. Xu, J Adv Res, 62 (2024) 143-154.
4 J.A. Grousd, H.E. Rich, J.F. Alcorn, Clin Microbiol Rev, 32 (2019).
5 W. Liu, R. Gao, C. Yang, Z. Feng, W. Ou-Yang, X. Pan, P. Huang, C. Zhang, D. Kong, W. Wang, Sci Adv, 8 (2022) eabn7006.
6 X. Hu, H. Zhang, Y. Wang, B.-C. Shiu, J.-H. Lin, S. Zhang, C.-W. Lou, T.-T. Li, Chem. Eng. J, 450 (2022).
7 C. Elian, R. Méallet, D.-L. Versace, Adv. Funct. Mater, 34 (2024) 2407228.
8 X. Qi, Y. Xiang, E. Cai, X. Ge, X. Chen, W. Zhang, Z. Li, J. Shen, Coordin Chem Rev, 496 (2023).
9 Y. Chen, Y. Gao, Y. Chen, L. Liu, A. Mo, Q. Peng, J Control Release, 328 (2020) 251-262.
10 S. Zhang, A. Wu, A. Ouyang, G. Lian, G. Ma, L. Wang, H. Guo, D. Zhang, J. Jiang, W. Liu, J. Mater. Chem. B, (2025).
11 T.Y. Wang, X.Y. Zhu, F.G. Wu, Bioact Mater, 23 (2023) 129-155.
12 J. Peng, K. Du, J. Sun, X. Yang, X. Wang, X. Zhang, G. Song, F. Feng, Angew Chem Int Ed, 62 (2023) e202214991.
13 X. Bi, Q. Bai, M. Liang, D. Yang, S. Li, L. Wang, J. Liu, W.W. Yu, N. Sui, Z. Zhu, Small, 18 (2022) e2104160.
14 S. Guan, S. Chen, X. Zhang, H. Zhang, X. Liu, Z. Hou, F. Wang, S. Qian, H. Zhu, J. Tan, X. Liu, Adv. Funct. Mater, 34 (2024) 2316093.
15 P. Manivasagan, T. Thambi, A. Joe, H.-W. Han, S.-H. Seo, Y. Jun Jeon, J. Conde, E.-S. Jang, Prog. Mater. Sci, 144 (2024).
16 J. Huo, Q. Jia, H. Huang, J. Zhang, P. Li, X. Dong, W. Huang, Chem. Soc. Rev.
17 F. Cui, T. Li, D. Wang, S. Yi, J. Li, X. Li, J Hazard Mater, 431 (2022) 128597.
18 S. Zhang, A. Wu, A. Ouyang, G. Lian, G. Ma, L. Wang, H. Guo, D. Zhang, J. Jiang, W. Liu, , Journal of Materials Chemistry B, (2025).
19 J. Sheng, Z. Zu, J. Qi, Y. Zhang, H. Wu, Z. Wang, Y. Miao, T. Zheng, S. Wang, L. Zhang, G. Lu, L. Zhang, Chem Eng J, 485 (2024).
20 W. Wang, G. Zhang, Y. Wang, J. Ran, L. Chen, Z. Wei, H. Zou, Y. Cai, W. Han, J Nanobiotechnol, 21 (2023) 367.
21 P. Zhao, Y. Zhang, X. Chen, C. Xu, J. Guo, M. Deng, X. Qu, P. Huang, Z. Feng, J. Zhang, Adv Sci, 10 (2023) e2206585.
22 L. Mei, Y. Zhang, K. Wang, S. Chen, T. Song, Mater Today Bio, 29 (2024) 101354.
23 L.E. Theune, J. Buchmann, S. Wedepohl, M. Molina, J. Laufer, M. Calderon, J Control Release, 311-312 (2019) 147-161.
24 J. Li, W. Zhang, W. Ji, J. Wang, N. Wang, W. Wu, Q. Wu, X. Hou, W. Hu, L. Li, J Mater Chem B, 9 (2021) 7909-7926.
25 H. Fu, K. Xue, Y. Zhang, M. Xiao, K. Wu, L. Shi, C. Zhu, Adv Sci, 10 (2023) e2206865.
26 Q. Ma, X. Sun, W. Wang, D. Yang, C. Yang, Q. Shen, J. Shao, Chinese Chem Lett, 33 (2022) 1681-1692.
27 X. Jiang, L. Wang, H. Tang, D. Cao, W. Chen, Dyes Pigments, 181 (2020).
28 G. Xu, Y. Song, H. Jin, P. Shi, Y. Jiao, F. Cao, J. Pang, Y. Sun, L. Fang, X.H. Xia, J. Zhao, Adv Sci (Weinh), (2024) e2407727.
29 L. Feng, C. Li, L. Liu, Z. Wang, Z. Chen, J. Yu, W. Ji, G. Jiang, P. Zhang, J. Wang, B.Z. Tang, ACS Nano, 16 (2022) 4162-4174.
30 S. Li, Q. Deng, Y. Zhang, X. Li, G. Wen, X. Cui, Y. Wan, Y. Huang, J. Chen, Z. Liu, L. Wang, C.S. Lee, Adv Mater, 32 (2020) e2001146.
31 A. Tang, C. Zhan, J. Yao, E. Zhou, Adv Mater, 29 (2017).
32 W. Zou, Y. Zhu, C. Gu, Y. Miao, S. Wang, B. Yu, Y. Shen, H. Cong, J Mater Sci, 55 (2020) 9918-9947.
33 L. Yuan, Y. Su, B. Yu, Y. Shen, H. Cong, Biomater Sci, 11 (2023) 985-997.
34 F. Bu, X. Kang, D. Tang, F. Liu, L. Chen, P. Zhang, W. Feng, Y. Yu, G. Li, H. Xiao, X. Wang, Bioact Mater, 33 (2024) 341-354.
35 X. Cheng, C. Zhang, K. Shen, H. Liu, C. Bai, Q. Ding, M. Guan, J. Wu, Z. Tian, D. Chen, L. Cai, X. Hong, Y. Xiao, Chem Eng J, 446 (2022).
36 C. Li, W. Zhang, S. Liu, X. Hu, Z. Xie, ACS Appl Mater Interfaces, 12 (2020) 30077-30084.
37 X. Yu, J. Zhao, X. Ma, D. Fan, Chem Eng J, 465 (2023).
38 F.W. Xia, B.W. Guo, Y. Zhao, J.L. Wang, Y. Chen, X. Pan, X. Li, J.X. Song, Y. Wan, S. Feng, M.Y. Wu, Adv Mater, 35 (2023) e2309797.
39 S.G.V. Charlton, A.N. Bible, E. Secchi, J.L. Morrell-Falvey, S.T. Retterer, T.P. Curtis, J. Chen, S. Jana, Adv Sci (Weinh), 10 (2023) e2207373.
40 D. Xian, R. Luo, Q. Lin, L. Wang, X. Feng, Y. Zheng, L. Lin, J. Chi, Y. Yan, G. Quan, T. Peng, Z. Xu, C. Wu, C. Lu, Mater Today Bio, 31 (2025) 101498.
41 X. Duan, J. Li, S. Huang, A. Li, Y. Zhang, Y. Xue, X. Song, Y. Zhang, S. Hong, H. Gao, Z. Wu, X. Zhang, Chem Eng J, 477 (2023)

View Article Online
DOI: 10.1039/D5TB01048A

The data supporting this article have been included as part of the Supplementary Information.